

◇ MONOGRAPH EXCERPT ◇

MATTER ANTIMATTER FLUCTUATIONS

SEARCH, DISCOVERY AND ANALYSIS OF B_s FLAVOR OSCILLATIONS

NUNO LEONARDO

Complete work published as:

Analysis of B_s oscillations at CDF, MIT Thesis (2006)

Matter antimatter fluctuations, Monograph, LAP Lambert (2011)

Author © Nuno Teotónio Leonardo

Chapter 10

Observation of B_s oscillations

In this chapter all of the ingredients previously developed are gathered to successfully achieve the first B_s oscillation measurement and firm observation.

10.1 Emergence of the B_s oscillation signal

In this section the novel SST method is applied to the sample of fully-reconstructed B_s decays in the 355 pb^{-1} dataset. The parameterized PID algorithm presented in Section 9 is employed to provide per-event predicted dilutions, based on the Monte Carlo calibration achieved in the previous chapter. The analysis procedures are those presented in Chapter 8. The method for combining flavor tagging information is that presented in Section 7.3.3. The signal likelihood factor $L_{\mathcal{D}}$ for the SST is provided by dilution templates obtained from the Monte Carlo samples.

The hadronic scan, where only statistical uncertainties are represented, is shown in Figure 10.1. The increase in sensitivity is very large, as anticipated, following the considerable improvement in tagging power brought about by the inclusion of the same-side tagging method. A value of 18.2 ps^{-1} in sensitivity is achieved, while the lower exclusion limit is 13.9 ps^{-1} . The updated combined world average scan, shown in Figure 10.2, is dominated by these results. The exclusion limit and 95% C.L. sensitivity obtained with this combined scan become 16.6 ps^{-1} and 21.7 ps^{-1} , respectively.

In the probed frequency spectrum all values are practically excluded except in the range of $(16.6, 18.2)\text{ ps}^{-1}$. This corresponds to a signature consistent with B_s oscillations, at about 17.5 ps^{-1} , where the amplitude value is largest. At that frequency, the measured amplitude significantly deviates from the background hypothesis, $\mathcal{A} = 0$, by 3.2 standard deviations. A more complete evaluation will be required to estimate the probability that a background fluctuation could mimic the observed signal signature.

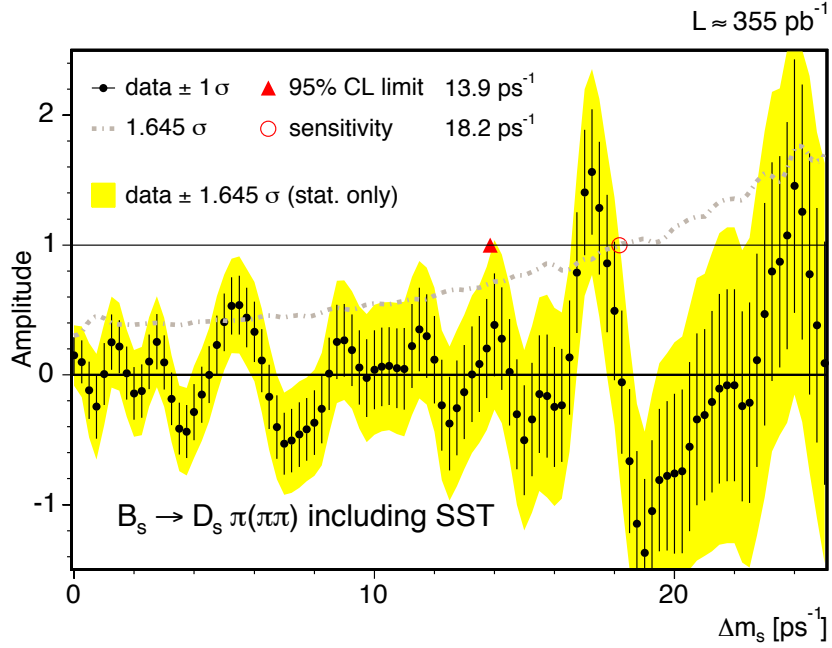


Figure 10.1: Updated amplitude scan for the hadronic modes, obtained with the addition of the parameterized PID SST algorithm; uncertainties are statistical only.

10.2 Extended dataset and first direct measurement

Having observed the rather striking oscillation signature in the previous section, the plan currently is to extend the analysis in the following two, rather obvious ways. First, the analysis is applied to the partially-reconstructed $B_s \rightarrow D_s l$ decays in addition to the fully-reconstructed $B_s \rightarrow D_s \pi(\pi\pi)$ modes, just as was done in Chapters 7 and 8. Second, the analysis is applied for the first time to the full dataset, which in reality was being further accumulated and processed while the analysis continued to be developed and polished, corresponding to an integrated luminosity of 1 fb^{-1} .

The tagging information is obtained from both same-side and opposite-side algorithms. The combined power of the opposite-side methods amounts to $\epsilon \mathcal{D}^2 = 1.5 \pm 0.1\%$. For the same-side algorithm, for which the effectiveness increases with the B_s p_T , the integrated tagging power $\epsilon \mathcal{D}^2$ is estimated to be 3.5% for the hadronic modes and 4.0% for the semileptonic modes. When both tags are present, their information is combined as described in Section 7.3.3, similarly to what was already done in Chapter 7 for the B^0 case and in Section 10.1 above for the B_s case.

The amplitude scan is shown in Figure 10.3. The signature for the oscillation found in Section 10.1 is now further reinforced, with the considerably larger sensitivity of 25.8 ps^{-1}

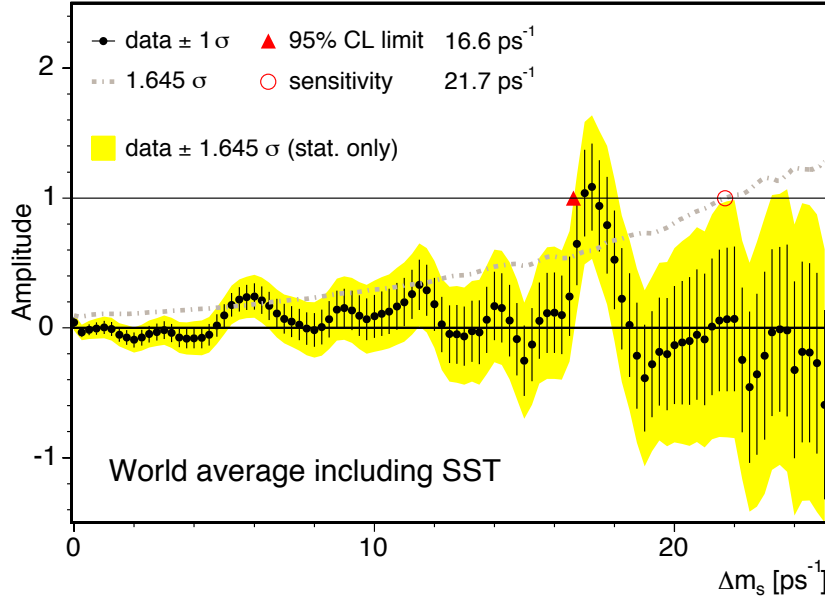


Figure 10.2: Combination of the hadronic scan of Figure 10.1 with the semileptonic and world average scans; statistical uncertainties only.

which is here attained, well above the signal region. The peak frequency is found at about $\Delta m_s = 17.3 \text{ ps}^{-1}$. The amplitude measurement at that frequency point yields $\mathcal{A} = 1.03 \pm 0.28$, being thus compatible with the signal hypothesis ($\mathcal{A} = 1$) and inconsistent with the non-oscillation hypothesis ($\mathcal{A} = 0$): $\mathcal{A}/\sigma_{\mathcal{A}} = 3.7$. The negative amplitudes measured at frequencies slightly below and above the peak frequency are expected, as discussed in Appendix .5.

Having determined the signal region via the amplitude scanning method, and under the hypothesis that the observed signal corresponds to B_s oscillations, we can in fact fit directly for the oscillation frequency. This is precisely what was also done in Chapter 7 when measuring the oscillation frequency in the B^0 system. There, we have introduced dilution calibration factors in the fit procedure. Presently, we rely on the flavor-tagging calibrations previously achieved, in Chapters 6, 7, and 8, and set $\mathcal{A} = 1$. In fact, the observed unit amplitude at the signal peak in the scan of Figure 10.3 further demonstrates the appropriate calibrations achieved in the previous chapters.

The measured B_s oscillation frequency is:

$$\Delta m_s = 17.31_{-0.18}^{+0.33}(\text{stat.}) \pm 0.07(\text{syst.}) \text{ ps}^{-1}.$$

The only significant systematic uncertainty on the Δm_s measurement, unlike for the amplitude measurement, is the uncertainty on the absolute scale of the proper decay time deter-

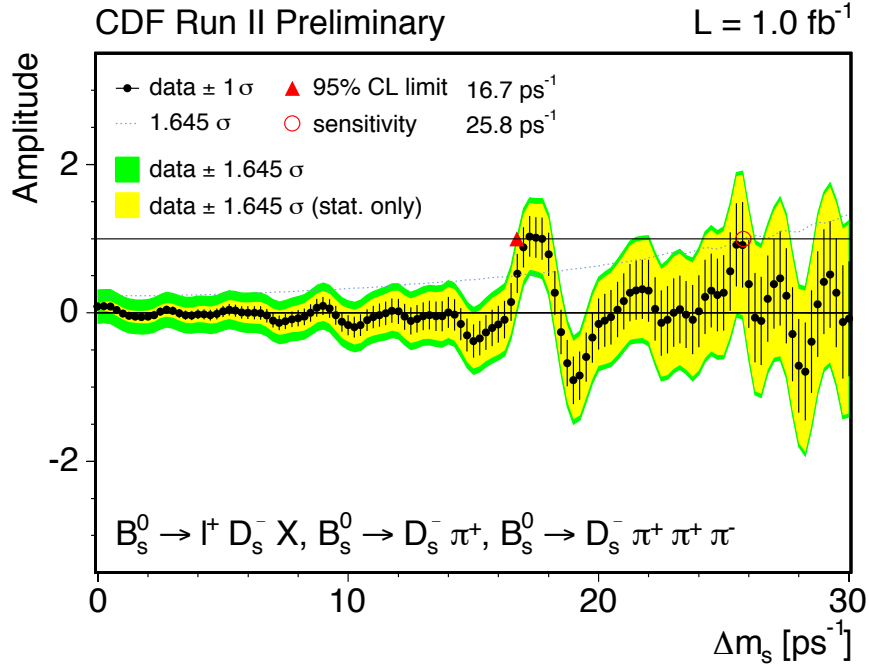


Figure 10.3: Amplitude scan yielding the first B_s oscillation frequency measurement, with 1 fb^{-1} .

mination. The main corresponding uncertainty sources include biases in the primary-vertex reconstruction and track fitting and alignment of the silicon detectors.

The likelihood profile is shown in Figure 10.4. On the left plot a comparison is made with the average likelihood values expected from the same equivalent dataset with and without B_s oscillations; these are further explained in Chapter 12.3. On the right plot, the likelihood profile is shown in the vicinity of the observed signal peak. The shape is found not to be exactly Gaussian, which is also reflected on the asymmetric uncertainty. From the likelihood plot, the following measured ranges at different confidence levels can be inferred:

$$\Delta m_s \in (17.01, 17.84) \text{ ps}^{-1} \text{ at } 90\% \text{ C.L.},$$

$$\Delta m_s \in (16.96, 17.91) \text{ ps}^{-1} \text{ at } 95\% \text{ C.L..}$$

Also shown on the right plot of Figure 10.4 are the separate contributions from the fully-reconstructed hadronic modes and the partially-reconstructed semileptonic modes. As anticipated for such a high frequency, the contribution of the former is dominant, owing to the superior proper-decay time resolution, while the latter provides the strongest constraint for $\mathcal{A} = 0$ for the lower frequency range of the amplitude spectrum of Figure 10.3.

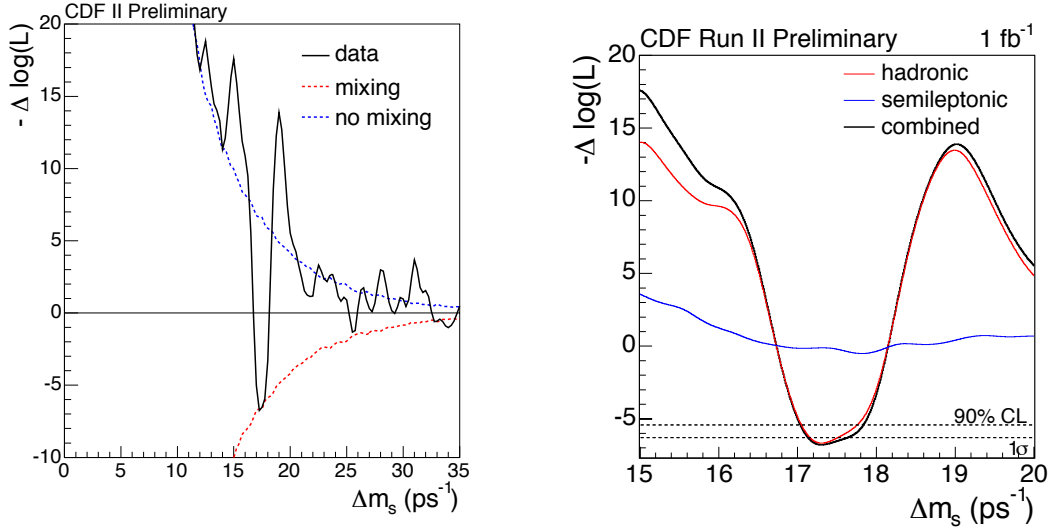


Figure 10.4: Likelihood profile for the first measurement of Δm_s , with a comparison to the values expected from equivalent data with and without B_s oscillations (left), and separate contributions from hadronic and semileptonic modes (right).

10.3 Further improvements and observation

Having further confirmed the initial oscillation signal and performed the world's first direct measurement of Δm_s , we currently aim at further establishing the observed signal as being indeed due, beyond reasonable doubt, to B_s oscillations in the data. For this purpose, a number of possible additional final optimizations will be explored and implemented, to allow to extract yet higher sensitivities from the dataset.

In the sample composition study performed in Section 4.3.2, it was noted the presence of incompletely-reconstructed hadronic decay modes, appearing to the left of the main B_s peak in mass spectrum. See also Figures 4.5, 4.6, and 4.8. The choice was initially made, *e.g.* in Chapter 5, to discard these contributions, either as background to the main signal or excluding the mass region below $5.3 \text{ GeV}/c^2$. Here however these get rehabilitated as full signal components, for the main reconstructed $B_s \rightarrow D_s[\phi\pi]\pi$ decay mode [64]. These contributions correspond to the $B_s \rightarrow D_s\rho$ and $B_s \rightarrow D_s^*\pi$ decays, where $\rho^+ \rightarrow \pi^+\pi^0$ and $D_s^* \rightarrow D_s^-\gamma$ or $D_s^-\pi^0$, and the soft neutral γ and π^0 are neglected in the reconstruction. Figure 10.5 shows the mass distribution of the main, fully-reconstructed B_s peak along with the incompletely-reconstructed components. The procedure for including the latter in the mixing analysis is identical to what has been employed for the semileptonic modes. In particular, the incompletely-reconstructed B_s momentum is accounted for in the PDF model by a distribution $\mathcal{F}(\kappa)$ of the fractional missing momentum, κ -factor; see (5.8) and Sec-

tion 5.3.2. The κ -factor distribution for all partially-reconstructed B_s decay modes employed in the analysis is shown on the right plot of Figure 10.5. As can be seen, the κ distribution is better localized for the $B_s \rightarrow D_s \rho$ and $B_s \rightarrow D_s^* \pi$ modes than it is for the $B_s \rightarrow D_s l$ modes, indicating in fact an effective resolution which does not degrade considerably relative to that of the fully-reconstructed peak. In addition, the kaon likelihood formed from dE/dx and TOF combined information (9.2), which was successfully explored already as part of the same-side tagger algorithm development in Chapter 9, is now also employed to find kaons from D_s meson decays. In the case of the hadronic modes, this additional observable is further combined with the previous selection criteria in a more effective fashion by employing an ANN implementation, as referred in Chapter 4. The resulting improved selection allows the additional decay mode $B_s \rightarrow D_s[\pi\pi\pi]\pi\pi\pi$ to also be included. The final signal yields extracted from the full 1 fb^{-1} dataset was presented in Section 4.4, where the corresponding mass distributions for each B_s mode are also shown.

In Section 7.2, the various opposite-side tagging algorithms were hierarchically ranked based on the highest expected performance for the event. An ANN implementation is here used to combine the tagging information from the various opposite-side algorithms. The fractional performance enhancement achieved in $\epsilon\mathcal{D}^2$ relative to the exclusive combination is about 15%. The kaon identification technique is also explored to look in opposite-side jets for kaons from the decay sequence $b \rightarrow c \rightarrow s$; such an opposite-side kaon tagger [65] contributes $\epsilon\mathcal{D}^2 \sim 0.2\%$. The total tagging power from the ANN-combined opposite-side methods amounts to $\epsilon\mathcal{D}^2 = 1.8 \pm 0.1\%$. The updated analysis of B^0 oscillations, described in Chapter 7 and applied to the full 1 fb^{-1} dataset, is illustrated in Figure 10.10(a) and yields

$$\Delta m_d = 0.510 \pm 0.009(\text{stat.}) \pm 0.016(\text{syst.}) \text{ ps}^{-1}.$$

An enhancement of the same-side algorithm was also investigated by using an ANN to combine the kaon-identification likelihood with the kinematic quantities of the track candidate [63]. The fractional $\epsilon\mathcal{D}^2$ gain obtained relative to the baseline implementation presented in Chapter 9 is about 10%. The tagging power of the same-side flavor-tagging method is observed to be $\epsilon\mathcal{D}^2 = 3.7\%$ for the hadronic, and $\epsilon\mathcal{D}^2 = 4.8\%$ for the semileptonic modes.

The updated combined amplitude scan is shown in Figure 10.6. The overall sensitivity attained is 31.3 ps^{-1} . The amplitude measurement at the frequency peak 17.75 ps^{-1} is $\mathcal{A} = 1.21 \pm 0.20$, found to be consistent with unit, denoting the correct calibration of the flavor taggers, and inconsistent with $\mathcal{A} = 0$: $\mathcal{A}/\sigma_{\mathcal{A}} = 6$. A comparison of selected amplitude scan contributions is displayed in Figures 10.7 and 10.8. The sensitivity and amplitude significance ($\mathcal{A}/\sigma_{\mathcal{A}}$ measured at 17.75 ps^{-1}) is 19.3 ps^{-1} and 1.8 for the semileptonic modes alone, and 30.7 ps^{-1} and 4.4 for the hadronic modes alone. The amplitude significance $\mathcal{A}/\sigma_{\mathcal{A}}$, measured

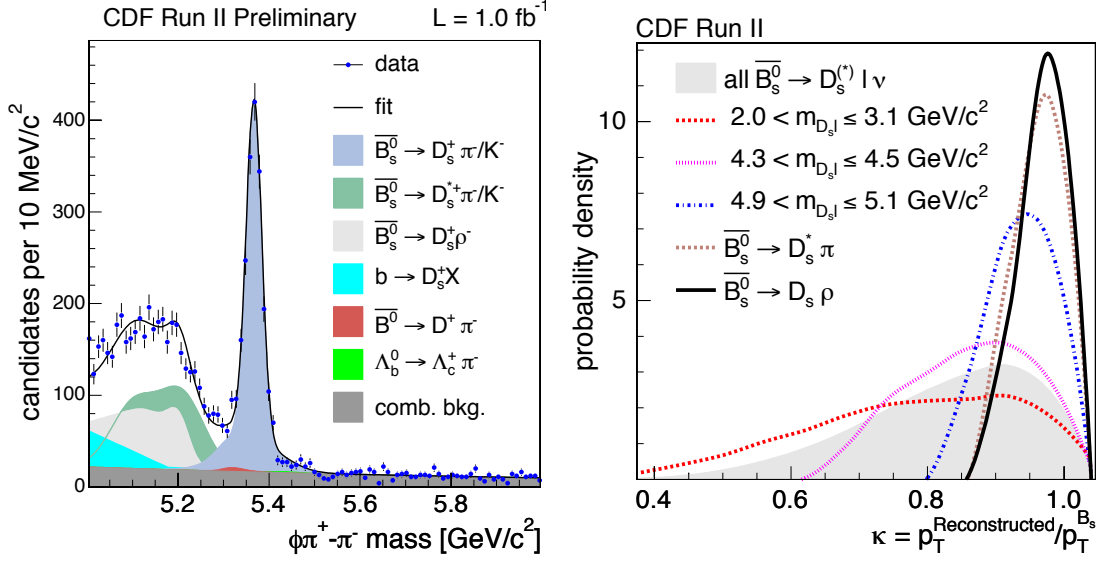


Figure 10.5: (Left) Mass distribution for the reconstructed $B_s \rightarrow D_s[\phi\pi]\pi$ modes including the contributions from $B_s \rightarrow D_s\rho$ and $B_s \rightarrow D_s^*\pi$ decays. (Right) κ -factor distributions for the semileptonic and hadronic partially-reconstructed modes.

at the same peak frequency, for partially-reconstructed hadronic modes is 1.8, and for the fully-reconstructed modes is 3.2. The sensitivity achieved with only the opposite-side taggers is 25.5 ps^{-1} and with the same-side tagger alone is 30.3 ps^{-1} .

The measured B_s oscillation frequency is:

$$\Delta m_s = 17.77 \pm 0.10(\text{stat.}) \pm 0.07(\text{syst.}) \text{ ps}^{-1}.$$

The likelihood profile is displayed in Figure 10.9. The combined shape, which is dominated by the fully-reconstructed hadronic modes, is symmetric and Gaussian. The contributions from the partially-reconstructed decays are also shown. From the likelihood plot, the following measured ranges at different confidence levels are inferred:

$$\Delta m_s \in (17.56, 17.96) \text{ ps}^{-1} \text{ at } 90\% \text{ C.L.},$$

$$\Delta m_s \in (16.51, 18.00) \text{ ps}^{-1} \text{ at } 95\% \text{ C.L..}$$

The B_s oscillation signal is depicted in Figure 10.10(b) as a function of decay time modulo the measured oscillation period $2\pi/\Delta m_s$.

10.4 Résumé

The introduction of the same-side tagging method in the analysis of the 355 pb^{-1} dataset yields a signature compatible with the B_s oscillation signal. At the frequency peak at about 17.5 ps^{-1} the significance $\mathcal{A}/\sigma_{\mathcal{A}}$ is about 3. Extending the analysis to the full dataset, of 1 fb^{-1} integrated luminosity, an increased sensitivity of 25.8 ps^{-1} is achieved, and the signature is confirmed, with an amplitude significance of $\mathcal{A}/\sigma_{\mathcal{A}} \sim 4$. The world's first direct measurement of Δm_s is performed.

Several optimizations are attempted toward further increasing the sensitivity to the oscillation signal. These include the addition of partially-reconstructed hadronic modes, an extended use of the kaon-identification technique, and introduction of an artificial neural network implementation for enhancing candidate selection and flavor-tagging combination. The sensitivity achieved is 31.3 ps^{-1} , yielding an amplitude significance of $\mathcal{A}/\sigma_{\mathcal{A}} \sim 6$.

The precise measurement of the B_s oscillation frequency is

$$\Delta m_s = 17.77 \pm 0.10(\text{stat.}) \pm 0.07(\text{syst.})\text{ ps}^{-1}.$$

The subject of the significance of the oscillation signal is next explored in Chapter 11, where a definitive confirmation of the observed signal will be further quantified. The impact of the measurement on theory models is addressed in Chapter 12.

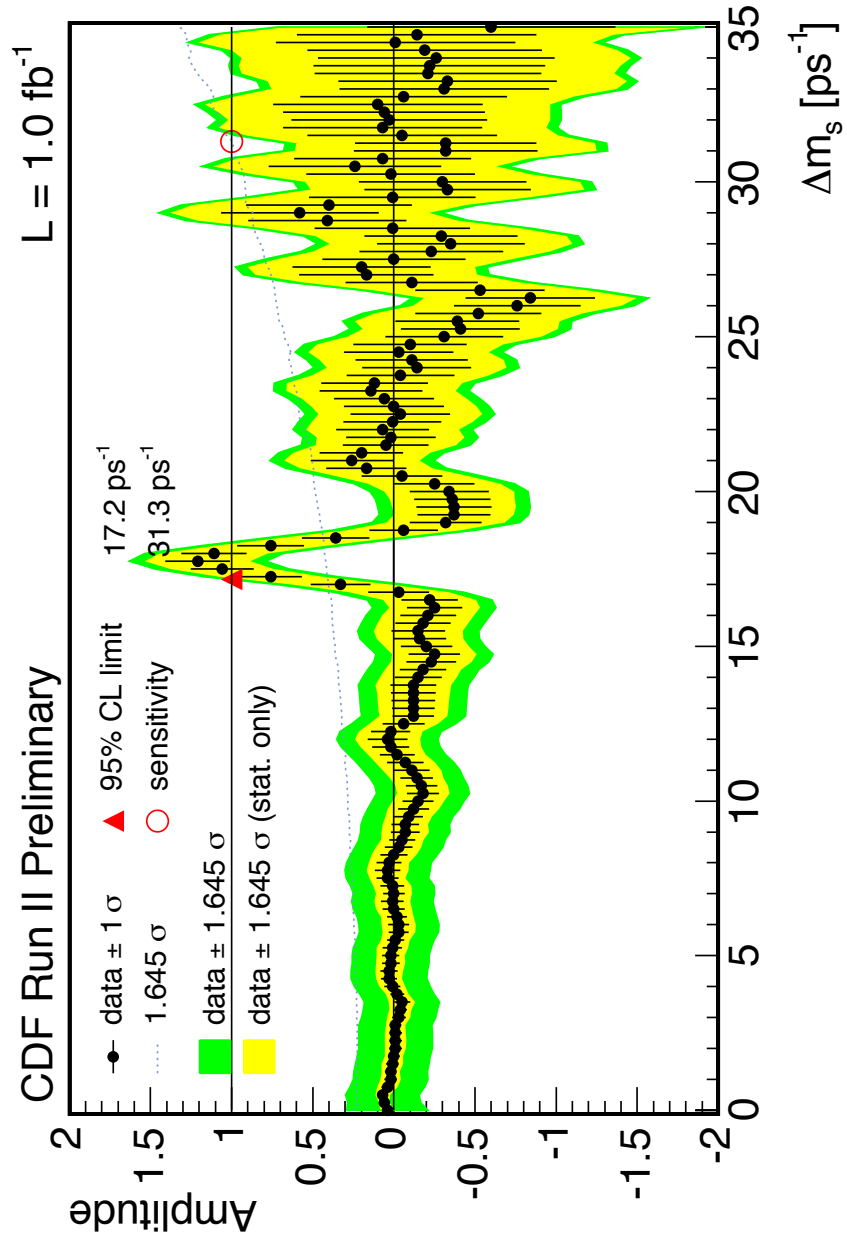


Figure 10.6: The combined amplitude scan yielding the first B_s oscillation observation.

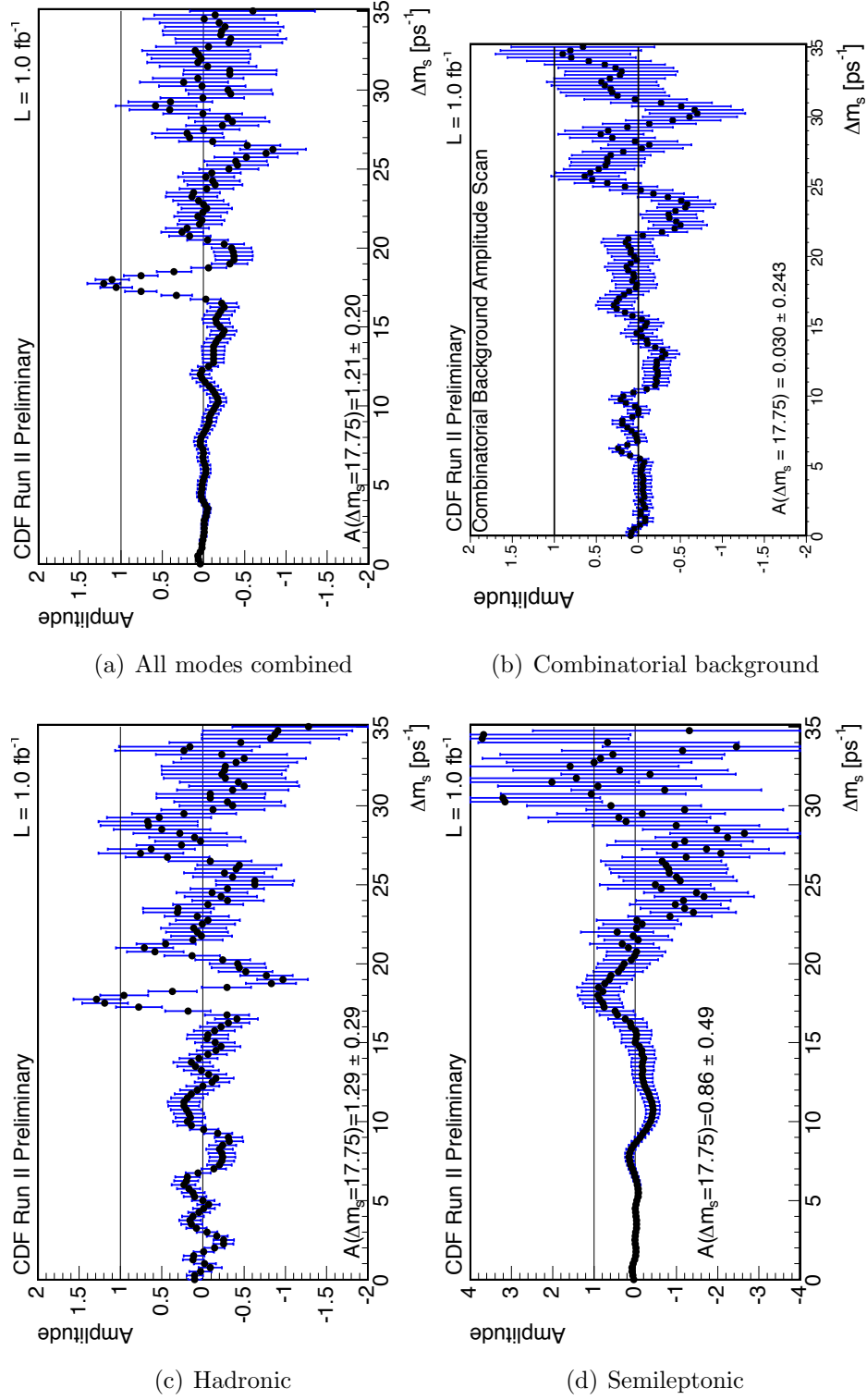


Figure 10.7: Comparison of amplitude scans contributing to the B_s oscillation observation; uncertainties are statistical only.

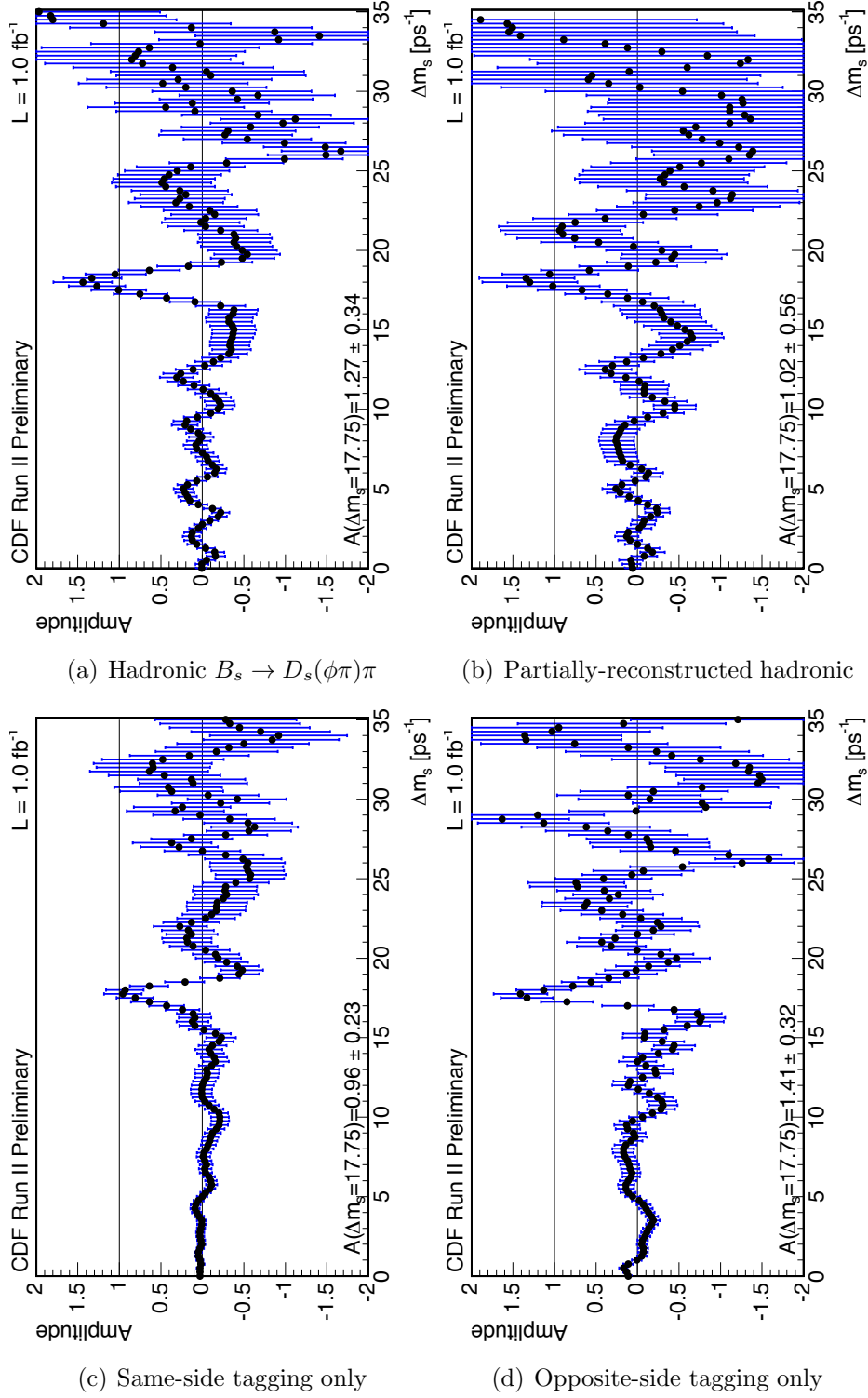


Figure 10.8: Comparison of amplitude scans from different decay types and tagging methods; uncertainties are statistical only.

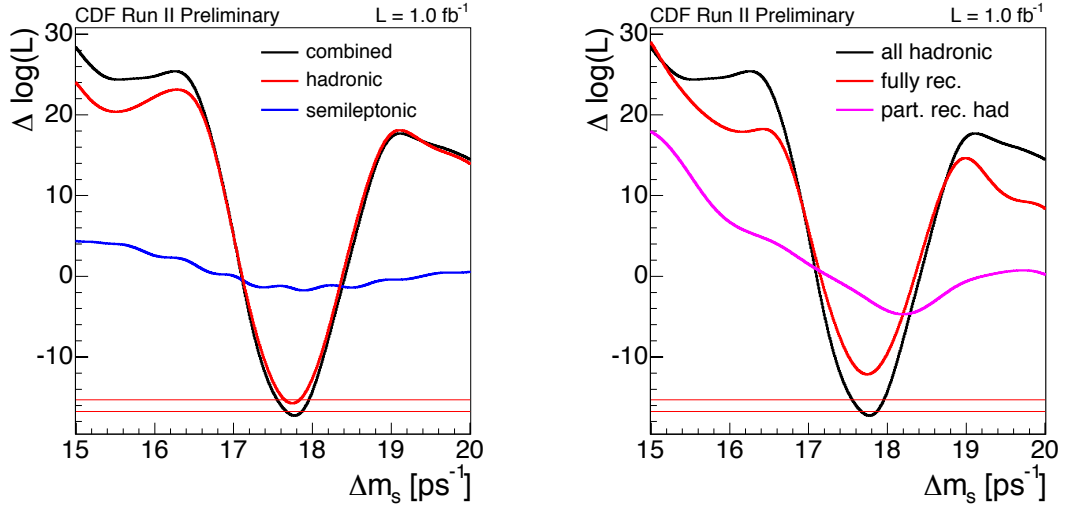


Figure 10.9: Likelihood profile for the B_s oscillation observation, with a comparison of semileptonic, partially- and fully-reconstructed hadronic modes; the horizontal lines indicate the 1σ and 95% C.L. intervals.

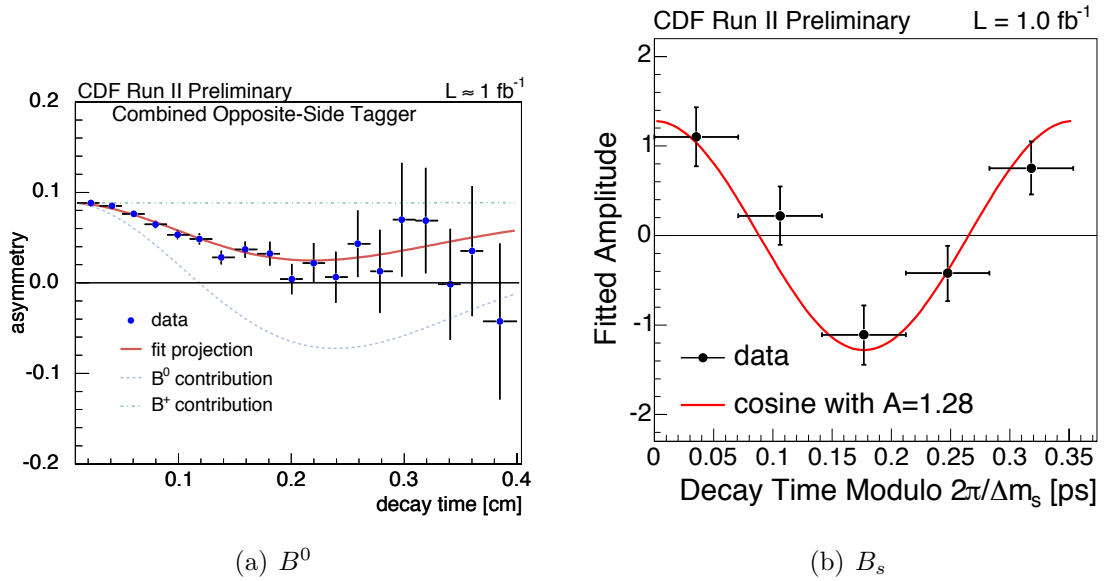


Figure 10.10: (Left) Time domain oscillation plot from the updated B^0 opposite-side tagging calibration analysis with 1 fb^{-1} , see Figure 7.1. (Right) The B_s oscillation signal depicted also as a function of decay time, modulo the measured oscillation period $2\pi/\Delta m_s$.